Scripta Materialia 201 (2021) 113953

Contents lists available at ScienceDirect

Scripta Materialia

journal homepage: www.elsevier.com/locate/scriptamat

Lattice distortion in selective laser melting (SLM)-manufactured unstable β-type Ti-15Mo-5Zr-3Al alloy analyzed by high-precision X-ray diffractometry

Aya Takase[a,b,*], Takuya Ishimoto[b], Ryoya Suganuma[b], Takayoshi Nakano[b,**]

[a] Rigaku Americas Corporation, 9009 New Trails Drive, The Woodlands, TX 77381, USA
[b] Division of Materials and Manufacturing Science, Graduate School of Engineering, Osaka University, 2-1, Yamadaoka, Suita, Osaka 565-0871, Japan

ARTICLE INFO

Article history:
Received 29 September 2020
Revised 21 March 2021
Accepted 19 April 2021

Keywords:
Selective laser melting (SLM)
β-type titanium alloys
Crystal structure
Residual stresses
X-ray diffraction (XRD)

ABSTRACT

A peculiar lattice distortion in a selective laser melting (SLM)-manufactured unstable β-type Ti-15Mo-5Zr-3Al was observed for the first time, through high-precision X-ray diffraction (XRD) analyses. After SLM, Ti-15Mo-5Zr-3Al exhibited a body-centered-tetragonal structure instead of a body-centered-cubic structure; the *c*-axis was 0.63% shorter than the *a*-axis. The XRD analyses also revealed tensile residual stresses of 210 ± 12 MPa at the specimen surface. A numerical simulation indicated rapid cooling during the SLM, which could have caused the residual stresses. A comparison of the partially stress-released SLM specimen and an electron beam melting-manufactured specimen with negligible residual stress suggested that the residual stress caused by the rapid cooling in SLM induced the lattice distortion. This finding is not consistent with the previous understanding that residual stress changes the lattice parameter without lattice distortion. This study provides new insight into lattice distortion generated by a combination of SLM-specific ultrarapid cooling and unstable phases.

β-type Ti alloys with body-centered-cubic (bcc) structures are a promising material for biomedical applications. Their excellent biocompatibility and uniquely low Young's modulus [1,2] are beneficial for suppressing stress shielding. The low Young's modulus results from the instability of the bcc phase (β-phase). The β-phase is likely to transform into other phases, such as the α-, ω-, and α"-phases, induced by applied stress and/or thermal history, depending on the β-phase instability [2–5]. Although a permanent transition of the major phase is not desirable, a partial or reversible phase transition can be beneficial. For example, the stress-induced martensitic α" phase transition that promotes twinning-induced plasticity has recently attracted attention [6,7].

Additive manufacturing (AM) is being researched as an effective method to fabricate customized parts with complex shapes. Powder-bed fusion, especially the selective laser melting (SLM) method, is suitable for fabricating small parts with complicated shapes, and its application for biomedical implants has been extensively researched [8,9]. SLM is characterized by repeated heating/cooling cycles resulting from laser scans with a small distance between its scan paths (scan pitch); the heating/cooling rates are somewhat high [10]. This unique thermal history can be detrimental to the crystalline phase stability, crystallographic texture, and residual stress [9–14]. One of the benefits of AM is its ability to fabricate the final part via a single process; therefore, we cannot rely on conventional methods used for wrought alloys, such as hot- and cold-rolling, to manipulate the crystal structures. Instead, it is necessary to understand the effects of the process parameters and thermal history on the crystalline structures and to optimize those parameters to control the final products.

Techniques such as electron backscatter diffraction and transmission electron microscopy are used to investigate crystalline phases and structures. However, the resolution of the interatomic spacing measurements in these techniques is limited to approximately 0.5 Å [15] or 15% of a typical metal lattice parameter. Contrarily, X-ray diffraction (XRD) is remarkably sensitive to interatomic spacing changes. In this study, we used high-precision XRD (HP-XRD) to investigate small changes in unstable β-phase crystalline structures undetectable using conventional techniques. HP-XRD combines parallel-beam geometry, whole-pattern fitting (WPF), and high-precision systematic peak-position correction to achieve a lattice distortion sensitivity of 0.02% [16,17]. We fabri-

* Corresponding author: Aya Takase, Tel: +1-760-594-4830
** Corresponding author: Takayoshi Nakano, Tel: +81-6-6879-7505
E-mail addresses: aya.takase@mat.eng.osaka-u.ac.jp (A. Takase), nakano@mat.eng.osaka-u.ac.jp (T. Nakano).

https://doi.org/10.1016/j.scriptamat.2021.113953

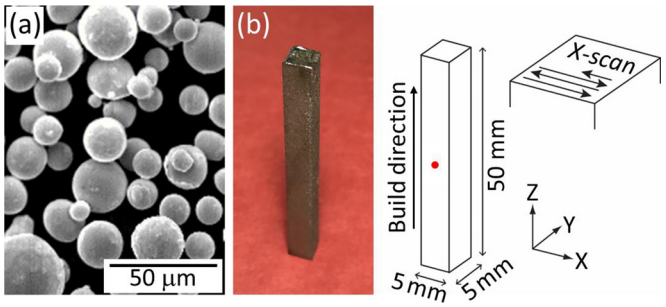

Fig. 1. (a) SEM image of gas-atomized Ti-15Mo-5Zr-3Al powder and (b) appearance and dimensions of SLM part. The red dot indicates the measurement location. The coordinate axes are also shown.

cated a Ti-15Mo-5Zr-3Al (mass%) part using SLM and investigated the lattice parameters of the β-phase to determine whether the rapid cooling process caused any phase transitions, lattice distortions, or residual stress.

The powder for SLM was prepared from Ti-15Mo-5Zr-3Al ingots using Ar gas-atomization (OSAKA Titanium Technologies, Japan). The obtained powder particles were spherical (Fig. 1(a)), and the median particle size was 31.6 μm. For the SLM fabrication, we used an EOS M290 (EOS, Germany) equipped with an Yb fiber laser. A specimen with dimensions of 5 mm (width) $\times$ 5 mm (depth) $\times$ 50 mm (height) was fabricated by scanning the laser beam parallel to the X-axis in alternating directions, as depicted in Fig. 1(b) [13,18]. The laser power, scanning speed, and scanning pitch were set to 360 W, 1200 mm/s, and 100 μm, respectively. The chemical composition of the specimen was determined using inductively coupled plasma (ICP) analysis. We analyzed the center of the XZ surface using HP-XRD.

The X-ray diffraction pattern was measured using a SmartLab diffractometer (Rigaku Corporation, Japan). To focus on the center area of the 5 mm-long laser-beam path, we shaped the incident X-ray beam to 1 mm $\times$ 2 mm, with the 2 mm side parallel to the specimen's Z-axis. We used parallel-beam geometry and the standard reference LaB_6 powder—NIST SRM 660c (National Institute of Standards and Technology, USA), certified by the National Institute of Standards and Technology [19]—for systematic peak-shift correction. For WPF, we employed the Pawley method to refine the lattice parameters precisely [20].

The same experimental setup was used to measure the residual stress to maintain the analyzed volume. We conducted $\sin^2\psi$ residual-stress measurements following the ASTM E915-10 [21] and SAE International [22] standards. The horizontal and vertical components of the residual stress were measured at the specimen surface using the β-phase (321) reflection at approximately 124.0° for 11 different ψ values.

Because a rapid cooling rate is the primary cause of residual stresses [9,14], we performed a finite-element analysis to estimate the cooling rate by simulating the heat transfer during the SLM process under the aforementioned laser condition. We used COMSOL Multiphysics® 5.5 (COMSOL, USA) for the calculations. The dimensions of the finite-element model were 5 mm (width) $\times$ 5 mm (depth) $\times$ 2 mm (height), and the same process parameters that were used to fabricate the SLM-made specimen were applied to the calculation. To simulate the three-dimensional energy distribution, we assumed that the heat flux from the laser beam exhibits a Gaussian distribution [23–25] and set the radius of the laser beam to 50 μm [26,27]. The penetration depth of the laser beam was adjusted based on the melt-pool dimensions [28,29]. The temporal and spatial heat transfer is governed by the following equation [30,31]:

$$\rho C \frac{\partial T}{\partial t} + \nabla \cdot \boldsymbol{q} = Q \quad (1)$$

Table 1
Thermal properties used in the simulation

Property	Value [unit]
Solidus temperature	1998 [K]
Liquidus temperature	2018 [K]
Density	5010 [kg/m^3]
Thermal conductivity of solid	21 [W/m•K]
Thermal conductivity of liquid	29 [W/m•K]
Specific heat capacity of solid	670 [J/kg•K]
Specific heat capacity of liquid	730 [J/kg•K]
Latent heat	370 [kJ/kg]

where ρ is the material density, C is the specific heat capacity, T is the temperature, t is the time, $\boldsymbol{q}$ is the heat flux vector, and Q is the amount of heat generated per unit volume. The latent heat was incorporated into the temperature dependence of the specific heat capacity [32,33]. Table 1 shows the thermal properties used in the simulation. The material density was set to 5010 kg/m^3 [34], and the liquidus and solidus temperatures were calculated using JMatPro® Version 9.1 (Sente Software, UK). Because the thermal conductivity, specific heat capacity, and latent heat of Ti-15Mo-5Zr-3Al are undefined, the corresponding values for Ti-6Al-4V were used instead [35].

Fig. 2(a) shows the diffraction pattern of the powder, which was identical to that of the bcc β-phase, with the lattice parameter refined to 3.2647 $\pm$ 0.0002 Å. The weighted profile R-factor (R_{wp}) was 10.59; a smaller R_{wp} indicates a better fit. Fig. 2(b) shows the diffraction pattern of the as-grown SLM-manufactured specimen. Since the composition of this specimen (wt%) was Mo 15.0, Zr 5.00, Al 2.98, and O 0.19 according to the ICP measurement, the specimen was expected to be composed of the β-phase. From a cursory observation, the SLM specimen appears to be in the bcc β-phase. However, the WPF analysis result based on the bcc structure revealed systematic discrepancies between the measurement and calculation; the R_{wp} was 15.34, significantly higher than the corresponding value for the powder. In fact, a comparison between the peak shapes obtained from the powder and the SLM specimen, with a peak around $2\theta = 97°$ as an example (Fig. 2(d)), shows that the peak of the SLM specimen splits into multiple peaks.

Microstructural parameters, such as the shape and size of the grains, affect only the broadening and intensities of diffraction peaks. The peak splitting was possibly caused by the lowered crystal symmetry. The body-centered-tetragonal (bct) structure has a lower symmetry than the bcc structure does, and the amount of peak split depends on the (h k l) combination. For example, (222) is not affected by this symmetry change, whereas the (200)–(002) and (310)–(103) combinations are significantly affected. This splitting of specific reflections, caused by distortion of the cubic structure, explains the systematic discrepancies observed in Fig. 2(b). The discrepancies indicate that the bcc structure in the SLM specimen was distorted and became a bct structure.

To consider the possibility of the compositional fluctuation contributing to the transformation to the bct phase, the compositional distribution was measured using energy-dispersive X-ray spectroscopy (Astec 3.1, Oxford Instruments, UK) in the region within ~40 μm from the sample surface in consideration of the X-ray penetration depth. An electron backscatter diffraction (EBSD) analysis (NordlysMax^3 system, Oxford Instruments, UK) was also performed in the same region to identify the crystal grains. A uniform chemical composition was observed (Fig. 3 and Table 2), indicating no element partitioning. Therefore, the formation of the bct phase was not considered to be due to compositional fluctuation. Thus, the WPF analysis was performed assuming that the specimen was composed of a bct single phase.

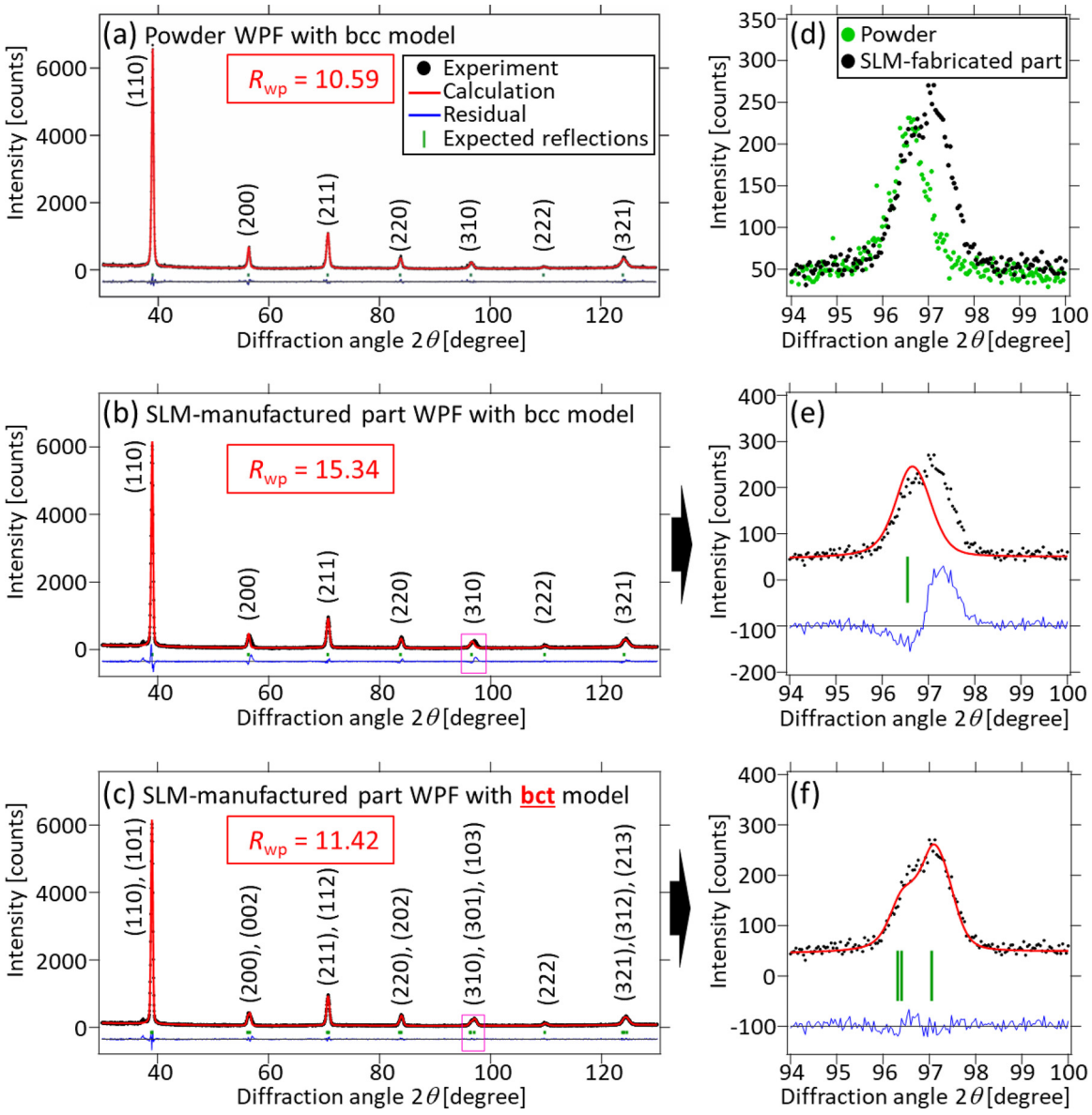

Fig. 2. Whole-pattern fitting of (a) powder with the bcc model, (b) SLM part with the bcc model, and (c) SLM part with a bct model. (d) Comparison of the diffraction peak around $2\theta = 97°$ between the powder and SLM part. (e, f) Magnified images of the regions delineated by the pink rectangles in (b) and (c). The XRD pattern for powder is well-fitted with the bcc model, whereas that for SLM specimen is well-fitted with the bct model.

Table 2
Differences in chemical composition among the seven grains

	Ti [wt%]	Mo [wt%]	Zr [wt%]	Al [wt%]
Average	76.90	14.91	5.25	2.94
Standard deviation	0.092	0.061	0.054	0.054
Coefficient of variation	0.001	0.004	0.010	0.018

Upon introducing the bct model, the systematic discrepancies in the WPF analysis disappeared, and R_{wp} decreased from 15.34 to 11.42. The (310) peak split was reproduced better by the bct model (Fig. 2(f)) than by the bcc model (Fig. 2(e)). Based on the WPF analysis, the lattice parameters were refined to $a = 3.2697 \pm 0.0001$ Å and $c = 3.2491 \pm 0.0001$ Å, exhibiting a 0.63% distortion calculated as $(a - c)/a \times 100$.

We sought to determine the possible causes of the lattice distortion observed in the SLM specimen. The ICP analysis showed that the specimen contained 0.19 wt% oxygen. Oxygen is known to stabilize the β-phase [36], and single-phase β Ti-15Mo-5Zr-3Al with up to 0.195 wt% oxygen has been reported [37]. Therefore, impurity is unlikely to have caused the distortion. This leaves the extremely rapid temperature change (heating/cooling) and the resultant residual stress as potential stabilizers of the bct phase.

To estimate the residual stress, which generally contributes to changes in the lattice parameter [22], we performed a $\sin^2\psi$ residual stress measurement on the same volume as that used for the WPF analysis. The residual stresses of the as-grown SLM specimen in the horizontal and vertical directions were estimated to be 210 $\pm$ 12 MPa and 260 $\pm$ 28 MPa in tension, respectively. The lattice distortion and residual stress coexisted in the specimen, suggesting the possibility of the residual stress being the cause of the lattice distortion. To verify this hypothesis, additional analysis was performed by changing the residual stress state using two methods. One involved sectioning the specimen to change the equilibrium of the stress state. We carefully prepared a 1.5 mm-thick section from the original surface of the SLM specimen. The constituent phase and residual stress were analyzed both on the original surface and internal side. The other method involved fabricating and measur-

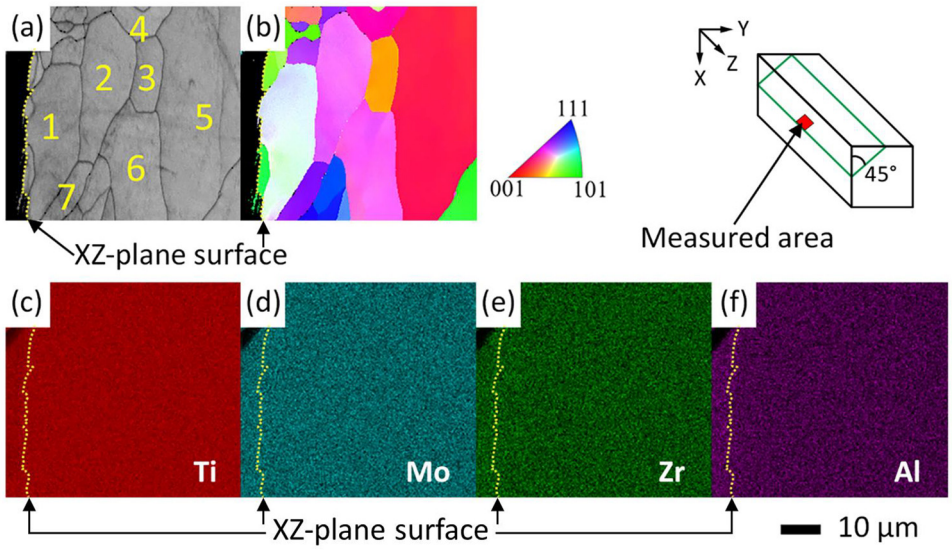

Fig. 3. (a) EBSD band contrast image and (b) inverse pole figure images for the representation of grains, and elemental distribution of (c) Ti, (d) Mo, (e) Zr, and (f) Al in the same area as in (a, b). Uniform elemental distribution was observed over the multiple grains. The measurement was performed on the surface where the HR-XRD and residual stress measurements were performed within the range of the X-ray penetration depth. The measurement surface was prepared at an angle of 45° (see inset) to analyze the surface area of the sample; therefore, a signal from outside the measurement surface was detected (the yellow dotted line in all figures indicates the specimen surface). The compositions of the seven crystal grains shown in (a) were analyzed (Table 2).

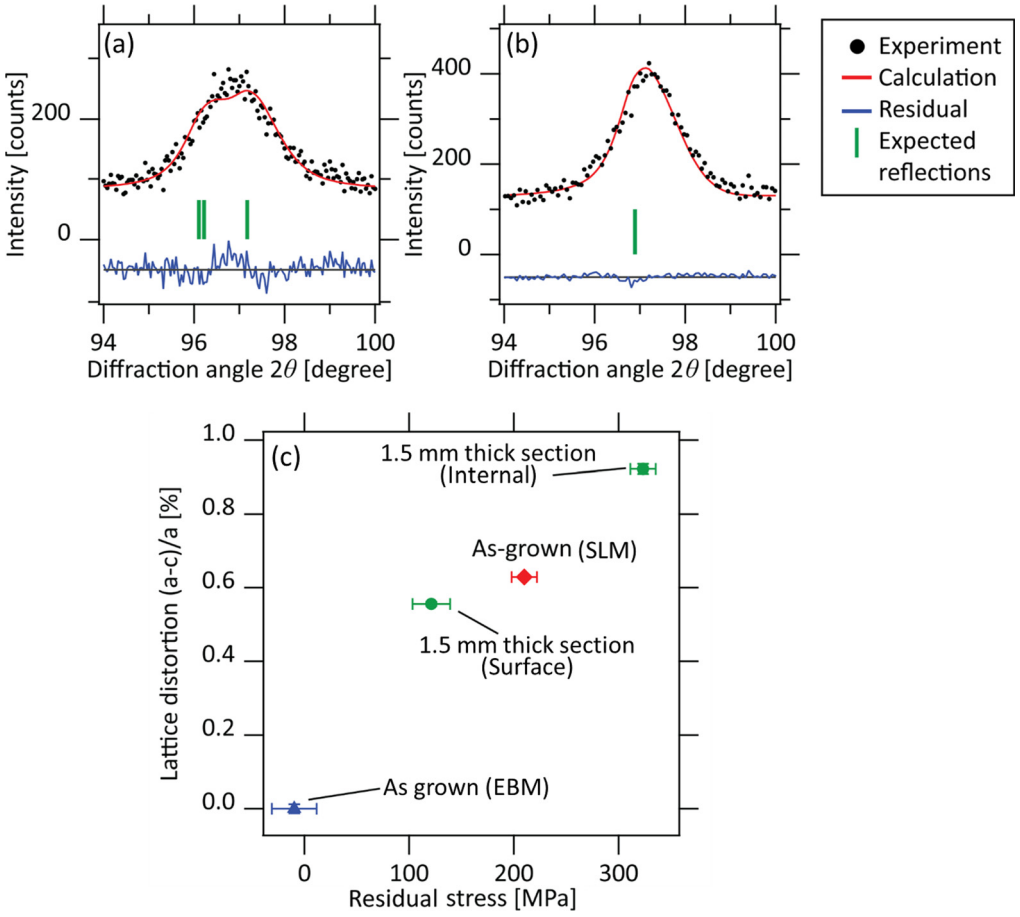

Fig. 4. (a) WPF result of 1.5 mm-thick section (internal) of the SLM specimen showing the split of the bct (310), (301), and (103) reflections, and (b) that of the EBM specimen showing the single bcc (310) reflection. (c) Plot of lattice distortion $(a - c)/a$ [%] versus residual stress. A strong correlation is observed between the two parameters.

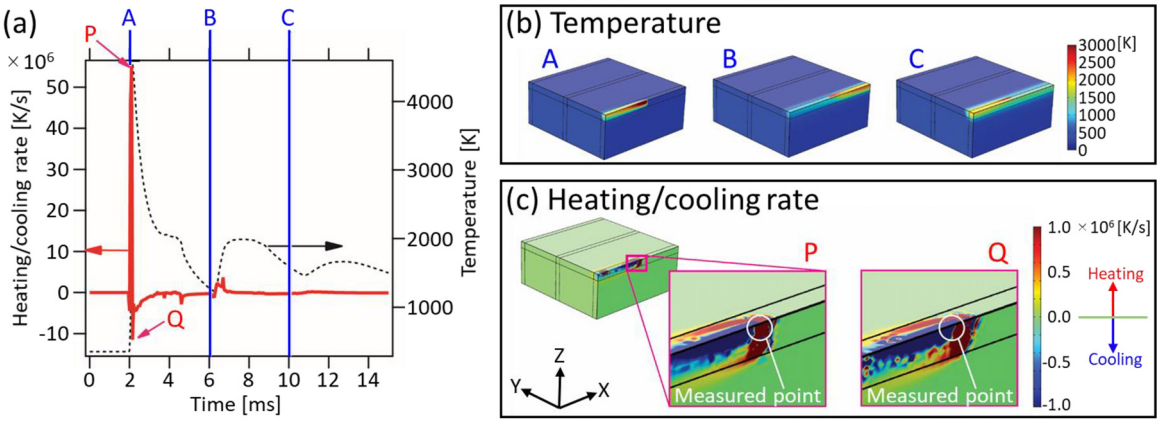

Fig. 5. Simulated temperature and heating and cooling rates. (a) Change in temperature and heating/cooling rate with laser scanning. (b) Temperature distribution at time points **A, B**, and **C**, at which the laser beam passes the center of the XZ plane. (c) Distribution of heating/cooling rate at points **P** and **Q**, at which the heating and cooling rates peaked.

ing an electron beam melting (EBM)-manufactured specimen with dimensions identical to those of the SLM specimen to investigate the "almost free from residual stress" state. It is well-known that in EBM, pre-heating causes almost no residual stress [38]. We used an Arcam Q10 (Arcam, Sweden) with an electron beam current and scan speed of 15 mA and 5000 mm/s, respectively. In terms of the scan strategy and scan pitch, the same conditions as those for SLM were used. The powder bed was pre-heated to 520°C.

The sectioned SLM specimen exhibited the same type of peak splitting for specific (h k l) combinations, indicating a bct structure. A representative WPF result for the internal side of the sectioned specimen is shown in Fig. 4(a). The bct model improved R_{wp} by 25–40% compared with the bcc model. The EBM specimen did not exhibit any (h k l) specific peak broadening and was accurately modeled with the bcc structure, as shown in Fig. 4(b).

The sectioned SLM specimen exhibited reduced residual stresses on the surface but significantly greater residual stresses on the internal side; however, this does not represent the as-grown state. The EBM specimen showed negligible residual stress. A comparison of the two specimens revealed a strong correlation between the degree of lattice distortion and the residual stress ($R^2 = 0.93$, $P < 0.05$), as shown in Fig. 4(c). It was proved that the residual stress generated during the SLM process was the main cause of the lattice distortion.

To estimate the temperature and heating and cooling rates experienced in the area analyzed via XRD, we performed a numerical simulation (Fig. 5). Animations of the simulated temperature and heating/cooling rate distributions are available in Supplementary Videos 1 and 2, respectively. **P** and **Q** in Fig. 5(a) are the points at which the heating and cooling rates peaked, respectively. The blue vertical lines in Fig. 5(a) indicate the time points (**A, B**, and **C**) at which the laser beam passed the center of the XZ plane, as shown in Fig. 5(b). From the second scan onward, the temperature near the XZ surface increased a few milliseconds after the laser beam passed, because the laser beam was 100 μm (equal to the scanning pitch) away. Moreover, the tail of the heated area caused the temperature increase, rather the scanned spot (an animation of this simulation is available). With the process parameters used to fabricate the specimens, the maximum cooling rate reached the order of 10^7 K/s. After the laser passed, a band-like region exhibiting a high cooling rate was formed (Fig. 5(c)). Immediately after solidification (between time points **A** and **B**), the cooling rate reached 3×10^6 K/s; thereafter, the heating and cooling rates repeatedly exceeded 10^5–10^6 K/s owing to multiple laser scans in the vicinity. This represents an extremely rapid temperature change. During cooling, the laser-irradiated area tended to shrink, but the shrinkage was constrained by the previously solidified layer underneath, leading to the generation of tensile residual stress. Residual stress is a form of restored energy in the crystal lattice and can induce a phase transition, as reported in the case of the β- and α"-phases [4,6,7]. For the specimens in this study, a strong correlation existed between the residual stress and lattice distortion, indicating that the residual stress was the primary cause of the distortion. Understanding how these factors are related requires a more systematic study of the lattice distortion and residual stresses in AM-processed parts using different techniques and process parameters. In general, residual stress changes the lattice spacing; however, our findings revealed the possibility that residual stress also changes crystal symmetry. This may be a unique phenomenon that has been discovered in an AM-processed metallic material with an unstable phase.

Several studies have investigated the phase and microstructures of AM-processed metallic materials [39,40], including those with unstable phases [12,41,42]; however, no detailed and quantitative studies on lattice distortion have been conducted. Lattice distortion can be a precursor to a phase transition, which may lead to undesired changes in the physicochemical properties of a material. Quantitatively investigating the level of distortion for different process parameters or at various locations on a specimen can provide valuable insight into the influence of those process parameters on the performance of the final components. This study thus serves as a template for analysis of AM-processed metal parts to investigate lattice distortion, including gradual changes in the lattice and intermediate states of, or precursors to, phase transitions.

Future research should clarify (1) the detailed mechanisms underlying the formation of the bct phase, (2) influence of the presence of the bct phase on physicochemical properties, and (3) how the bct phase undergoes further phase transformation under the condition employed, e.g., under stress. In general, post-heat-treatment enables the reduction of residual stress and non-equilibrium phases. However, detecting changes in micro- and ultra-structures—whether desirable or not—without post-treatment is important to avoid offsetting the benefits of the net-shape-fabrication ability of SLM.

Declaration of Competing Interest

The authors declare that they have no known competing financial interests or personal relationships that could have appeared to influence the work reported in this paper.

Acknowledgments

This work was supported by the Grants-in-Aid for Scientific Research (JP18H05254) from the Japan Society for the Promotion of Science (JSPS). This work was also partly supported by the Cross-Ministerial Strategic Innovation Promotion Program (SIP), Materials Integration for Revolutionary Design System of Structural Materials, Domain C1: “Development of Additive Manufacturing Process for Ni-based Alloy” from the Japan Science and Technology Agency (JST).

Supplementary materials

Supplementary material associated with this article can be found, in the online version, at doi:10.1016/j.scriptamat.2021.113953.

References

[1] S.-H. Lee, M. Todai, M. Tane, K. Hagihara, H. Nakajima, T. Nakano, J. Mech. Behav. Biomed. Mater. 14 (2012) 48–54.
[2] M. Tane, K. Hagihara, M. Ueda, T. Nakano, Y. Okuda, Acta Mater. 102 (2016) 373–384.
[3] L.-F. Huang, B. Grabowski, J. Zhang, M.-J. Lai, C.C. Tasan, S. Sandlöbes, D. Raabe, J. Neugebauer, Acta Mater. 113 (2016) 311–319.
[4] T. Inamura, H. Hosoda, K. Wakashima, S. Miyazaki, Mater. Trans. 46 (2005) 1597–1603.
[5] P. Wang, M. Todai, T. Nakano, J. Alloys Compd. 766 (2018) 511–516.
[6] Y. Fu, W. Xiao, D. Kent, M.S. Dargusch, J. Wang, X. Zhao, C. Ma, Scr. Mater. 187 (2020) 285–290.
[7] B. Chen, W. Sun, Scr. Mater. 150 (2018) 115–119.
[8] A. Sidambe, Materials 7 (2014) 8168–8188.
[9] L.-C. Zhang, H. Attar, Adv. Eng. Mater. 18 (2016) 463–475.
[10] T. DebRoy, H.L. Wei, J.S. Zuback, T. Mukherjee, J.W. Elmer, J.O. Milewski, A.M. Beese, A. Wilson-Heid, A. De, W. Zhang, Prog. Mater. Sci. 92 (2018) 112–224.
[11] T. Ishimoto, R. Ozasa, K. Nakano, M. Weinmann, C. Schnitter, M. Stenzel, A. Matsugaki, T. Nagase, T. Matsuzaka, M. Todai, H.S. Kim, T. Nakano, Scr. Mater. 194 (2021) 113658.
[12] B. Vrancken, L. Thijs, J.-P. Kruth, J. Van Humbeeck, Acta Mater. 68 (2014) 150–158.
[13] T. Ishimoto, K. Hagihara, K. Hisamoto, S.-H. Sun, T. Nakano, Scr. Mater. 132 (2017) 34–38.
[14] J.L. Bartlett, Addit. Manuf. 27 (2019) 131–149.
[15] R. Erni, M.D. Rossell, C. Kisielowski, U. Dahmen, Phys. Rev. Lett. 102 (2009) 096101.
[16] T. Mitsunaga, M. Saigo, G. Fujinawa, Powder Diffr. 17 (2002) 173–177.
[17] A. Takase, 60th Annu. Conf. Appl. X-Ray Anal. (2011) D81 D-.
[18] S.-H. Sun, T. Ishimoto, K. Hagihara, Y. Tsutsumi, T. Hanawa, T. Nakano, Scr. Mater. 159 (2019) 89–93.
[19] J.A. Small, R.L. Watters, Jr., Certificate SRM 660c. (2015). https://www-s.nist.gov/srmors/view_cert.cfm?srm=660C.
[20] G.S. Pawley, J. Appl. Crystallogr. 14 (1981) 357–361.
[21] ASTM Int. E 915 - 96 (2002).
[22] SAE_HS-784 (2003).
[23] H.J. Willy, X. Li, Z. Chen, T.S. Herng, S. Chang, C.Y.A. Ong, C. Li, J. Ding, Mater. Des. 157 (2018) 24–34.
[24] S. Liu, H. Zhu, G. Peng, J. Yin, X. Zeng, Mater. Des. 142 (2018) 319–328.
[25] G.L. Knapp, N. Raghavan, A. Plotkowski, T. DebRoy, Addit. Manuf. 25 (2019) 511–521.
[26] Q. Chen, X. Liang, D. Hayduke, J. Liu, L. Cheng, J. Oskin, R. Whitmore, A.C. To, Addit. Manuf. 28 (2019) 406–418.
[27] EOS M 290 – https://www.eos.info/en/additive-manufacturing/3d-printing-metal/eos-metal-systems/eos-m-290. Accessed 30th April 2021.
[28] A. Foroozmehr, M. Badrossamay, E. Foroozmehr, S. Golabi, Mater. Des. 89 (2016) 255–263.
[29] M.-S. Pham, B. Dovgyy, P.A. Hooper, C.M. Gourlay, A. Piglione, Nat. Commun. 11 (2020) 749.
[30] H.S. Carslaw, J.C. Jaeger, Conduction of Heat in Solids, 2nd ed., Oxford University Press, Oxford, 1986.
[31] Y. Li, D. Gu, Mater. Des. 63 (2014) 856–867.
[32] V. Pashkis, Trans AFS 53 (1945) 90.
[33] S.J. Wolff, S. Lin, E.J. Faierson, W.K. Liu, G.J. Wagner, J. Cao, Acta Mater. 132 (2017) 106–117.
[34] https://www.azom.com/article.aspx?ArticleID=9427. Accessed 30th April 2021.
[35] R. Rai, P. Burgardt, J.O. Milewski, T.J. Lienert, T. DebRoy, J. Phys. D: Appl. Phys. 42 (2009) 025503.
[36] S.-H. Lee, M. Todai, M. Tane, K. Hagihara, H. Nakajima, T. Nakano, J. Mech. Behav. Biomed. Mater. 14 (2012) 48–54.
[37] N. Nomura, T. Kohama, I.H. Oh, S. Hanada, A. Chiba, M. Kanehira, K. Sasaki, Mater. Sci. Eng. C 25 (2005) 330–335.
[38] H. Galarraga, R.J. Warren, D.A. Lados, R.R. Dehoff, M.M. Kirka, P. Nandwana, Mater. Sci. Eng. A 685 (2017) 417–428.
[39] W. Chen, C. Chen, X. Zi, X. Cheng, X. Zhang, Y.C. Lin, Mater. Sci. Eng. A 726 (2018) 240–250.
[40] J. Haubrich, J. Gussone, P. Barriobero-Vila, P. Kürnsteiner, E.A. Jägle, D. Raabe, N. Schell, G. Requena, Acta Mater. 167 (2019) 136–148.
[41] Y.J. Liu, S.J. Li, H.L. Wang, W.T. Hou, Y.L. Hao, R. Yang, T.B. Sercombe, L.C. Zhang, Acta Mater. 113 (2016) 56–67.
[42] L. Zhou, T. Yuan, J. Tang, L. Li, F. Mei, R. Li, Mater. Charact. 145 (2018) 185–195.